

Non-invasive ion fraction quantification of dual-species beams in low-energy synchrotrons

Elisabeth Renner,¹ Matthias Kausel,^{2,1} Hermann Fuchs,³ Katrin Holzfeind,¹ and Nana Okropiridze¹

¹*Atominstitut, TU Wien, Stadionallee 2, 1020 Vienna, Austria**

²*MedAustron, Marie-Curie Straße 5, 2700 Wiener Neustadt, Austria*

³*Medical University of Vienna, Spitalgasse 23, 1090 Vienna, Austria*

The ion composition of dual-species beams in synchrotrons is typically inferred from invasive measurements performed after beam extraction. This paper introduces a complementary non-invasive method to determine the ion composition of such beams directly inside the synchrotron. The approach is applicable to low-energy synchrotrons and to small relative mass-to-charge ratio offsets, typically at the 10^{-4} level. The method exploits dispersive orbit offsets between the two species and corresponding frequency corrections applied by the synchrotron RF radial regulation loop. This capability is of particular interest for ongoing research on online monitoring in carbon ion beam therapy using mixed ${}^4\text{He}^{2+}$ and ${}^{12}\text{C}^{6+}$ beams, which feature a mass-to-charge ratio offset of 0.065 %.

The proposed method is analytically derived and tested with particle tracking simulations using XSUITE. Its applicability under realistic experimental conditions is demonstrated at the MedAustron facility using mixed ${}^4\text{He}^{2+}$ and ${}^{12}\text{C}^{6+}$ beams. The results show good agreement with independent post-extraction measurements.

I. INTRODUCTION

In recent years, mixed helium and carbon ion irradiation has been proposed as a new concept for treatment monitoring in carbon ion beam therapy [1, 2]. Given their similar charge-to-mass ratio of $q/m \approx 0.5$, with a relative difference of

$$\frac{\Delta(m/q)}{(m/q)} = \frac{(m/q)_{\text{He}} - (m/q)_{\text{C}}}{(m/q)_{\text{C}}} = 6.5 \times 10^{-4}, \quad (1)$$

${}^4\text{He}^{2+}$ and ${}^{12}\text{C}^{6+}$ can be simultaneously accelerated and extracted for patient irradiation. Being extracted at the same energy-per-mass, ${}^4\text{He}^{2+}$ features approximately three times the range in matter of ${}^{12}\text{C}^{6+}$. By measuring the residual energy of the ${}^4\text{He}^{2+}$ ions in a detector located downstream of the patient, anatomical changes and patient alignment errors can be identified (Fig. 1).

Since 2023, both at GSI [3] and MedAustron [4], mixed helium and carbon ion beams have been successfully generated, accelerated, and extracted to the irradiation rooms for interdisciplinary research in accelerator

physics, detector development and medical physics. Due to differing accelerator capabilities, GSI currently generates the mixed beam directly in a single ion source [3], while at MedAustron the two ion species are generated in separate ion sources and mixed by means of a sequential multiturn injection into the synchrotron [4].

Currently, these beams are provided to research users on an experimental basis, with helium fractions

$$r = \frac{N_{\text{He}}}{N_{\text{He}} + N_{\text{C}}} \quad (2)$$

typically varying within $0.1 < r < 0.5$, depending on the specific user requirements. N_{He} and N_{C} are the intensities per species. Studies towards future clinical implementation currently consider helium fractions of $r \approx 0.1$ to 0.2 , as this range is expected to provide a ${}^4\text{He}^{2+}$ signal distinguishable from the ${}^{12}\text{C}^{6+}$ fragments, while the dose deposited by ${}^4\text{He}^{2+}$ amounts to less than 1 % of the total dose [2, 5]. However, final clinical target values and tolerances for the helium fraction have not yet been established.

In case of mixed beam generation in a single ion source, the helium fraction can be tailored by adjusting the helium gas flow to the ion source plasma [3]. In case of mixed beam generation in of a sequential multiturn injection, as done at MedAustron [4], it is possible to tailor the helium fraction using the injection settings (Sec. II A). However, particularly in the latter approach, the helium fraction can exhibit noticeable shot-to-shot fluctuations.

At present, the ion composition cannot be determined directly within the accelerator complex and is instead inferred from measurements of the extracted beam in the irradiation room. Such measurements require the installation of a dedicated diagnostic setup, which complicates beam commissioning tasks. Further, in most cases the setup cannot be installed simultaneously with experiments, which means that no cycle-resolved information on the delivered mixing ratio is available.

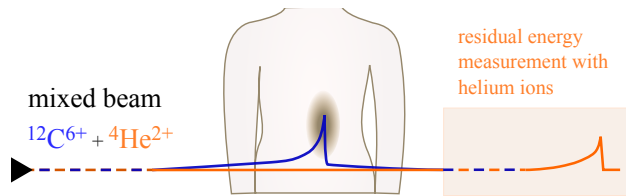


FIG. 1. Schematic mixed beam irradiation. The carbon beam is used for tumor treatment while the residual helium energy is measured downstream of the patient for diagnostic purposes.

* Contact author: elisabeth.renner@tuwien.ac.at

To address this gap, this work proposes a new non-invasive method for estimating the ion composition prior to extraction in synchrotrons. The method relies on composition-dependent feedback from the radial regulation loops of the synchrotron radio frequency (RF) system. Due to the small but measurable difference in beam rigidity between ${}^4\text{He}^{2+}$ and ${}^{12}\text{C}^{6+}$ (Sec. II B), the two ion species follow different dispersive orbits. In synchrotrons without radial RF regulation, information on the ion composition can be obtained from the measured orbit offset in dispersive regions. In synchrotrons with radial RF regulation it can be retrieved from the applied frequency corrections. While the present work focuses on the latter case, the methodology can in principle also be adapted to synchrotrons without radial regulation loops.

Section II reviews the status of mixed beam delivery at MedAustron as well as the RF acceleration of such beams. Section III presents the proposed method for determining the ion fraction in the synchrotron. The experimental demonstration is described in Sec. IV, followed by discussion and concluding remarks in Secs. V and VI.

II. BACKGROUND

A. Mixed ion beam delivery at MedAustron

At the MedAustron Ion Therapy and Research Center, which is based on the Proton-Ion Medical Machine Study (PIMMS) [6, 7], mixed helium-carbon ion beams are generated and delivered to the irradiation room for non-clinical research studies using a sequential multi-turn injection scheme [4]. In nominal single-species operation, helium and carbon ion beams are generated in two separate ion sources as ≈ 8 keV/u ${}^4\text{He}^{2+}$ and ${}^{12}\text{C}^{4+}$ beams, which are subsequently pre-accelerated through a radio frequency quadrupole and linear accelerator to ≈ 7 MeV/u. The beams then pass a stripping foil. The fully stripped ${}^4\text{He}^{2+}$ and ${}^{12}\text{C}^{6+}$ ions are injected into the synchrotron via a conventional multiturn injection.

In mixed-species operation, the beam is generated by successively injecting the ${}^4\text{He}^{2+}$ and ${}^{12}\text{C}^{6+}$ ions from the two distinct ion sources into the synchrotron. First, ${}^4\text{He}^{2+}$ ions are injected and stored at flat bottom. After this the injector is reconfigured and ${}^{12}\text{C}^{6+}$ is injected using a second multiturn injection. A substantial fraction of the already circulating ${}^4\text{He}^{2+}$ beam is lost at the injection septum when ramping the injection bump for the ${}^{12}\text{C}^{6+}$ injection. As a result, the two ion species end up occupying different regions in horizontal phase space. One way to tailor the ion fraction is to adjust the amplitude of the second injection bump [4].

Following sequential injection, both ion species are captured together and accelerated to extraction energies between 120 MeV/u and 402.8 MeV/u. As in standard operation, the synchrotron RF system [8] employs radial and phase regulation loops to verify the beam energy and RF phase. The system operates with a loop cycle time

of 10 μs . The two ion species are subsequently extracted together using third-order resonance slow extraction. To date, the clinically employed betatron core-driven slow extraction is not compatible with mixed-beam operation [4]. Therefore the mixed beam slow extraction has so far been performed with either RF knockout (RFKO) or phase displacement extraction (PDE), profiting from recent developments on these alternative slow extraction mechanisms at MedAustron [9–11].

B. RF acceleration of mixed-species ion beams

When accelerating mixed-species beams with slightly different q/m in synchrotrons the RF synchronism condition must be simultaneously fulfilled for all ion species despite the slightly different closed-orbit lengths. As a consequence, the secondary ion species attains a slight offset in momentum-per-mass from the reference species, as reviewed below.

The synchronous particle of the reference species (species I) is described using the rest mass m_{I} , charge q_{I} , velocity $v_{\text{I}} = \beta_{\text{I}} c$, with the speed of light c , and the relativistic factors β_{I} and γ_{I} . The synchronous particle of the secondary ion species (species II) is described using m_{II} , q_{II} , β_{II} and γ_{II} . Note that the synchronous particle of species I may be off-momentum with respect to the on-momentum reference particle, which is denoted by the subscript “0”. The label “sp” is used to indicate offsets between the two ion species.

The relative offset in magnetic rigidity $B\rho = \frac{m\gamma\beta c}{q}$ of species II from species I,

$$\begin{aligned} \frac{\Delta(B\rho)}{(B\rho)_{\text{I}}} &= \frac{\Delta(p/q)}{(p/q)_{\text{I}}} = \frac{m_{\text{II}}/q_{\text{II}}}{m_{\text{I}}/q_{\text{I}}} \cdot \frac{\beta_{\text{II}}\gamma_{\text{II}}}{\beta_{\text{I}}\gamma_{\text{I}}} - 1 \\ &= \delta_{\text{eff,sp}} \end{aligned} \quad (3)$$

depends on offsets in both, q/m and $p/m = \beta\gamma c$. Following the notation of Hermes et al. [12], it is also referred to as *effective relative momentum offset* δ_{eff} .

Similar to the mono-species case, the deviation in p/m , i.e. in $\beta\gamma$, is parametrized by

$$\delta_{\text{sp}} = \frac{\Delta(p/m)}{(p/m)_{\text{I}}} = \frac{\Delta(\beta\gamma)}{(\beta\gamma)_{\text{I}}} = \frac{\beta_{\text{II}}\gamma_{\text{II}}}{\beta_{\text{I}}\gamma_{\text{I}}} - 1. \quad (4)$$

The offset in q/m is commonly described by the factor

$$\chi_{\text{sp}} = \frac{q_{\text{II}}/m_{\text{II}}}{q_{\text{I}}/m_{\text{I}}}. \quad (5)$$

Together, Eqs. (4) and (5) are used to rewrite the relative rigidity offset between species I and II, Eq. (3), as

$$\delta_{\text{eff,sp}} = \frac{1 + \delta_{\text{sp}}}{\chi_{\text{sp}}} - 1. \quad (6)$$

The formalism presented in Sec. III is based on linearized models valid for small charge-to-mass ratio offsets

$|\chi_{\text{sp}} - 1| \ll 1$. Treating derivations in this work consistently to first order, Eq. (6) can be expressed as

$$\delta_{\text{eff,sp}} \approx \frac{1}{\chi_{\text{sp}}} - 1 + \delta_{\text{sp}}. \quad (7)$$

Due to this rigidity offset, the secondary ion species follows a different dispersive orbit than the reference ion species, with the modified average bending radius

$$R_{\text{II}} = R_{\text{I}} (1 + \alpha_c \delta_{\text{eff,sp}}) + \mathcal{O}(\delta_{\text{eff,sp}}^2), \quad (8)$$

where α_c is the linear momentum compaction factor. In case of off-momentum operation α_c is evaluated at the momentum offset of the reference species I.

When the RF system is turned on, both synchronous particles must have the same revolution frequency f_{rev} , despite their different closed-orbit lengths. This results in the two ion species acquiring slightly different β , i.e.

$$\begin{aligned} \frac{\Delta f_{\text{rev}}}{f_{\text{rev,I}}} = 0 &= \frac{\beta_{\text{II}} R_{\text{I}}}{\beta_{\text{I}} R_{\text{II}}} - 1 \\ &\Rightarrow \frac{\beta_{\text{II}}}{\beta_{\text{I}}} = \frac{R_{\text{II}}}{R_{\text{I}}}. \end{aligned} \quad (9)$$

Inserting Eq. (8), with Eq. (7), and

$$\frac{\beta_{\text{II}}}{\beta_{\text{I}}} \approx 1 + \frac{1}{\gamma_{\text{I}}^2} \delta_{\text{sp}} + \mathcal{O}(\delta_{\text{sp}}^2), \quad (10)$$

into Eq. (9) yields an expression for the relative offset in $p/m = \beta\gamma c$ of species II from species I,

$$\begin{aligned} \delta_{\text{sp}} &= \frac{(\beta\gamma)_{\text{II}} - (\beta\gamma)_{\text{I}}}{(\beta\gamma)_{\text{I}}} \\ &= \frac{\gamma_{\text{I}}^2}{\gamma_{\text{tr}}^2 - \gamma_{\text{I}}^2} \left(\frac{1}{\chi_{\text{sp}}} - 1 \right), \end{aligned} \quad (11)$$

with $\gamma_{\text{tr}} = 1/\sqrt{\alpha_c}$ being the transition energy. Alternatively, this expression can also be obtained by logarithmic differentiation, i.e.

$$\frac{d(p/q)}{(p/q)} = \frac{d(m/q)}{(m/q)} + \frac{d(\beta\gamma)}{(\beta\gamma)}, \quad (12)$$

as presented for example in references [13, 14].

As an example, we consider a mixed ${}^4\text{He}^{2+}/{}^{12}\text{C}^{6+}$ beam in a PIMMS-like synchrotron with $\alpha_c \approx 0.25$, operated below transition. ${}^{12}\text{C}^{6+}$ is defined as the reference species I. ${}^4\text{He}^{2+}$, species II, features $\chi_{\text{sp}} = 0.99935$. It is therefore slightly more rigid than ${}^{12}\text{C}^{6+}$ and follows an orbit with increased path length. This means that, below transition, ${}^4\text{He}^{2+}$ must be accelerated to slightly higher velocities, $\beta_{\text{He}} > \beta_{\text{C}}$, to ensure synchronism with the RF wave. The introduced relative offset in $\beta\gamma$ for ${}^4\text{He}^{2+}$ in such a synchrotron, Eq. (11), is between $\delta_{\text{sp}} \approx 0.3\text{‰}$ and 0.7‰ for clinical extraction energies per nucleon of $E_{\text{kin}} = 120\text{ MeV/u}$ to 400 MeV/u . This offset is comparable in magnitude to the operational rms

momentum spreads δ_{rms} at flat top, prior to an optional phase jump [15]. The related total effective rigidity offset, Eq. (7), ranges from 0.95‰ to 1.35‰ for the stated extraction energies [16].

Above transition, Eq. (11) changes sign and the resulting lower $\beta_{\text{II}} < \beta_{\text{I}}$ of the secondary ion species reduces the effective rigidity offset, Eq. (7). For $\gamma_{\text{I}} \gg \gamma_{\text{tr}}$, $\delta_{\text{sp}} \rightarrow (1 - 1/\chi_{\text{sp}})$, the two contributions in Eq. (7) compensate and $\delta_{\text{eff,sp}}$ vanishes. Both ion species move on the same orbit. However, it would not be possible to cross transition and keep both ion species in a mixed-species beam due to the above-described increasing rigidity difference and hence orbit separation when approaching transition energy. This effect was made use of in the late 1980s in the CERN PS to clean a S^{16+} beam from a O^{8+} contamination [14, 17].

III. ION FRACTION QUANTIFICATION

This section presents a model that exploits the described difference in beam rigidity between two ion species to non-invasively determine the mixing ratio. The model is applicable to low-energy synchrotrons, ion mixtures with small charge-to-mass offsets, $|\chi_{\text{sp}} - 1| = \mathcal{O}(10^{-4})$, and is formulated under the assumption that the horizontal dispersion is approximately constant for the respective rigidity offsets. Furthermore, it requires that the beam position monitors exhibit an approximately linear response across the horizontal range occupied by both ion species, allowing their signals to be superimposed. This condition is met by shoe-box type pick-ups [18].

A proposal conceptually related to the approach pursued here was put forward by S. van der Meer in 1978 [19]. He suggested determining the mass difference between p^+ and \bar{p}^+ in the CERN SPS by resolving their orbit separation in a dispersive region. However, this approach was ultimately not pursued, as subsequent analyses indicated that for that specific use case alternative methods could achieve higher accuracy [13, Chp. 7.7].

A. Dispersive distribution of mixed-species beams

For a dual-species beam with N_{I} ions of species I with charge $Q_{\text{I}} = q_{\text{I}} e$ (charge state q , elementary charge e) and N_{II} ions of species II with charge state q_{II} , it is useful to distinguish between the total number of ions

$$N_{\text{mix}} = N_{\text{I}} + N_{\text{II}}, \quad (13)$$

and the total number of charges

$$N_{\text{q,mix}} = N_{\text{I}} q_{\text{I}} + N_{\text{II}} q_{\text{II}}. \quad (14)$$

Using the previously introduced definition for the ion fraction

$$r = \frac{N_{\text{II}}}{N_{\text{II}} + N_{\text{I}}}, \quad (15)$$

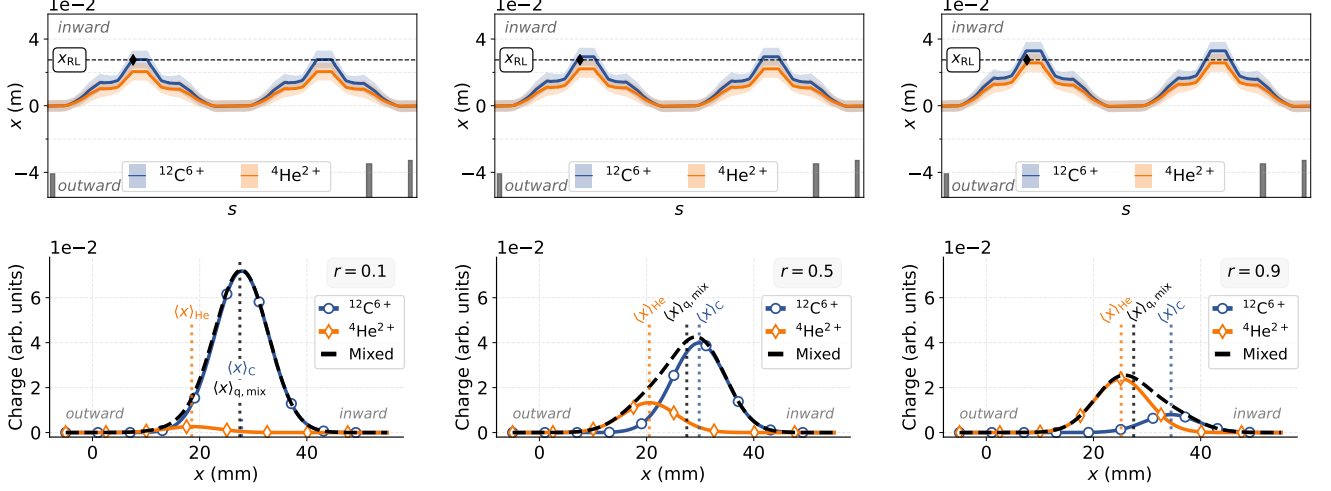


FIG. 2. Mixed ${}^4\text{He}^{2+}$ and ${}^{12}\text{C}^{6+}$ beam charge distributions for different helium fractions r . The radial loop regulates the horizontal center of gravity of the mixed charge distribution, $\langle x \rangle_{q,\text{mix}}$, to $x_{\text{RL}} = 27.5$ mm. Top: $1\sigma_{\text{rms}}$ beam envelopes along a PIMMS synchrotron. Bottom: Horizontal charge distributions at the radial loop pick-up with $D_x = -8.3$ m.

$N_{q,\text{mix}}$ can be expressed by

$$\begin{aligned} N_{q,\text{mix}} &= N_{\text{I}} q_{\text{I}} + N_{\text{II}} q_{\text{II}} \\ &= (1 - r) N_{\text{mix}} q_{\text{I}} + r N_{\text{mix}} q_{\text{II}} . \end{aligned} \quad (16)$$

At a location with non-zero horizontal dispersion $D_x \neq 0$, the center of gravity of species II features a horizontal offset from the center of gravity of species I of

$$\langle x \rangle_{\text{II}} - \langle x \rangle_{\text{I}} = D_x \delta_{\text{eff,sp}}, \quad (17)$$

with $\delta_{\text{eff,sp}}$ obtained from Eqs. (7) and (11). In case of off-momentum operation, with the reference ion species featuring a relative momentum offset δ_{I} (as common in a PIMMS-like synchrotron) D_x is the horizontal dispersion evaluated at the momentum offset of the reference ion species, i.e., $D_x = D_x(\delta_{\text{I}})$.

Consequently, the two displaced charge distributions shift the center of gravity position of the entire charge distribution to

$$\begin{aligned} \langle x \rangle_{q,\text{mix}} &= \frac{N_{\text{II}} q_{\text{II}} \langle x \rangle_{\text{II}} + N_{\text{I}} q_{\text{I}} \langle x \rangle_{\text{I}}}{N_{q,\text{mix}}} \\ &= A_r D_x \delta_{\text{eff,sp}} + \langle x \rangle_{\text{I}} , \end{aligned} \quad (18)$$

with the charge-weighted ion fraction

$$A_r = \frac{q_{\text{II}} r}{q_{\text{II}} r + q_{\text{I}} (1 - r)} . \quad (19)$$

To provide an example, Fig. 2 illustrates the charge distributions for a mixed 262.3 MeV/u ${}^4\text{He}^{2+}$ and ${}^{12}\text{C}^{6+}$ beam with different ion fractions r in a PIMMS [6, 7] lattice. ${}^{12}\text{C}^{6+}$ is considered the reference ion species. As in standard operation, the modeled synchrotron is operated off-momentum, with a radial loop correcting the RF

frequency so that the measured center of gravity of the total charge distribution, $\langle x \rangle_{q,\text{mix}}$, features the requested offset x_{RL} at the radial loop pick-up, in this example $x_{\text{RL}} = 27.5$ mm. The two distributions are separated by Eq. (17). In the convention used throughout this work, the beam moves counterclockwise and hence $x > 0$ and $x < 0$ denote horizontal offsets toward and away from the center of the synchrotron, respectively, which is indicated in Fig. 2 as *inward* and *outward*. ${}^4\text{He}^{2+}$, being more rigid, with $\delta_{\text{eff,sp}} > 0$ moves on a closed orbit shifted towards the outside of the synchrotron.

The top row displays the horizontal $1\sigma_{\text{rms}}$ beam envelopes of ${}^4\text{He}^{2+}$ (orange) and ${}^{12}\text{C}^{6+}$ (blue). The black dashed line marks the radial loop setpoint. The diamond marker indicates the dispersive location ($D_x = -8.3$ m) at which a representative pick-up is installed in this model. The envelope is computed as $\sigma_{\text{rms}} = \sqrt{\beta_x \epsilon_{x,n,\text{rms}} / (\gamma \beta) + D_x^2 \delta_{\text{rms}}^2}$, where β_x denotes the Courant-Snyder β -function. Both ion species are assumed to have Gaussian momentum distributions with similar rms momentum spreads of $\delta_{\text{rms}} \approx 0.5 \times 10^{-3}$ [15]. For this illustration, both ion species are further modeled with Gaussian betatron distributions with a normalized rms emittance of $\epsilon_{x,n,\text{rms}} = 0.9 \mu\text{m}$ [20]. While in practice, the horizontal emittances of ${}^4\text{He}^{2+}$ and ${}^{12}\text{C}^{6+}$ differ significantly when generating a mixed beam using a double multiturn injection scheme [4], this distinction is not relevant for the present analysis and is therefore omitted here for simplicity. The bottom row shows the respectively modeled horizontal charge densities at the location of the radial loop pick-up.

B. Radial loop regulation of mixed-species beams

The radial loop acts on the overall charge distribution (black-dashed line in the bottom row of Fig. 2) and applies a frequency correction $\Delta f(r) = f_{\text{mix}}(r) - f_{\text{ref}}$ to move $\langle x \rangle_{q,\text{mix}}$ to the specified radial loop setpoint. f_{mix} denotes the RF frequency of the mixed beam after regulation to the prescribed offset x_{RL} . f_{ref} is the corresponding reference frequency of a mono-isotopic beam of the reference ion species (only species I, i.e. $r = 0$), which is acquired at the same radial loop setpoint. In the remaining section, the subscript ‘‘ref’’ is omitted for describing this reference beam, i.e. $f \equiv f_{\text{ref}}$, $\gamma \equiv \gamma_{\text{ref}}$, $\beta \equiv \beta_{\text{ref}}$, $p \equiv p_{\text{I,ref}}$ and $R \equiv R_{\text{ref}}$.

Derivation A: After regulation, the displacement of the reference species I with respect to the mono-species reference position follows from Eq. (18) as

$$x_{\text{I}}(r) - x_{\text{RL}} = -A_{\text{r}}(r) D_x \delta_{\text{eff,sp}}. \quad (20)$$

This offset can be related to the induced momentum shift of species I, $\Delta p_{\text{I}} = p_{\text{I}} - p$, by

$$D_x \frac{\Delta p_{\text{I}}}{p} = -A_{\text{r}} D_x \delta_{\text{eff,sp}}. \quad (21)$$

D_x cancels out, assuming it is approximately constant over the relevant range. Finally, the obtained $\Delta p_{\text{I}}/p$ can be related to the required relative frequency offset,

$$\frac{\Delta f}{f} = -\eta A_{\text{r}} \delta_{\text{eff,sp}}, \quad (22)$$

with the slippage factor $\eta = 1/\gamma^2 - 1/\gamma_{\text{tr}}^2$. Rearranging with Eqs. (7) and (11) yields the relative frequency offset expected for a specific ion fraction r ,

$$\frac{\Delta f}{f} = -\frac{1}{\gamma^2} A_{\text{r}}(r) \left(\frac{1}{\chi_{\text{sp}}} - 1 \right). \quad (23)$$

Equivalently, the ion fraction r can be obtained from a measured $\Delta f/f$ by rearranging Eq. (23), yielding

$$r = \frac{q_{\text{I}} \gamma^2 \frac{\Delta f}{f}}{\gamma^2 \frac{\Delta f}{f} (q_{\text{I}} - q_{\text{II}}) - q_{\text{II}} \left(\frac{1}{\chi_{\text{sp}}} - 1 \right)}. \quad (24)$$

Notably, Eqs. (23) and (24) are independent of the machine layout. The reason becomes clear when deriving the same expressions using the alternative approach B.

Derivation B: In this method, we introduce a virtual particle representing the charge-weighted center of gravity of the mixed beam distribution. This virtual particle is described by an effective charge-to-mass ratio factor

$$\chi_{\text{v}}(r) = \frac{\chi_{\text{sp}} q_{\text{II}} r + q_{\text{I}} (1 - r)}{q_{\text{II}} r + q_{\text{I}} (1 - r)}. \quad (25)$$

Also this approach requires that D_x is approximately constant over the relevant range. Beyond the scope of the present work, significant higher-order dispersive terms may require the introduction of appropriate $\delta_{\text{eff,sp}}$ - and r -dependent weighting factors for the two terms of the numerator of Eq. (25). In that case, an explicit closed-form solution is not generally expected.

The radial loop regulates the dispersive offset of this virtual particle to the same position as the mono-isotopic reference beam. This means, that the effective rigidity offset of the virtual particle with respect to the reference beam vanishes,

$$\delta_{\text{eff,v}} = \frac{1}{\chi_{\text{v}}} - 1 + \delta_{\text{v}} = 0, \quad (26)$$

which requires the virtual particle to feature a relative offset in $\beta\gamma$ of

$$\delta_{\text{v}} = 1 - \frac{1}{\chi_{\text{v}}} \approx \chi_{\text{v}} - 1. \quad (27)$$

Since the radial loop aligns the center of gravity of the mixed beam with the reference orbit, the effective path length of the virtual particle equals that of the reference beam, i.e. $R_{\text{v}} = R$ in Eq. (9). Using Eq. (10), the relative frequency offset becomes

$$\frac{\Delta f}{f} = \frac{\beta_{\text{v}} R}{\beta R_{\text{v}}} - 1 = \frac{1}{\gamma^2} \delta_{\text{v}} + \mathcal{O}(\delta_{\text{v}}^2). \quad (28)$$

The measured relative frequency shift $\Delta f/f$ can therefore be used to estimate the relative offset in $p/m = \beta\gamma c$ of the virtual particle,

$$\delta_{\text{v}} \approx \gamma^2 \frac{\Delta f}{f}. \quad (29)$$

With Eqs. (25) and (27) one obtains again Eqs. (23) and (24), as presented with *derivation A*. It is now evident, that the derived relations are independent of the synchrotron optics, since no effective path length difference of the virtual particle is involved ($R_{\text{v}} = R$).

To provide an example, Fig. 3 illustrates the resulting relations for a mixed ${}^4\text{He}^{2+}$ and ${}^{12}\text{C}^{6+}$ beam in a PIMMS synchrotron lattice, with a pure ${}^{12}\text{C}^{6+}$ beam as the reference species. The example explores energies between 120 MeV/u and 1 GeV/u and ion fractions between $r = 0$ (pure ${}^{12}\text{C}^{6+}$) and $r = 1$ (pure ${}^4\text{He}^{2+}$). While this example assumes on-momentum operation for simplicity, the relations remain valid for off-momentum operation.

Notably, it is evident in Fig. 3 (left and center panels) that the method is not applicable for $\gamma \gg 1$ as the induced frequency offset vanishes in accordance with the $1/\gamma^2$ dependence in Eq. (23). This can be explained by the fact that above transition energy, the offset in $\beta\gamma$ between the two ion species, Eq. (11), changes sign. For $\gamma \gg 1$ the secondary ion species obtains exactly the δ_{sp} to compensate the rigidity offset introduced by $\chi_{\text{sp}} \neq 1$. The two ion species do not move on separate orbits; the

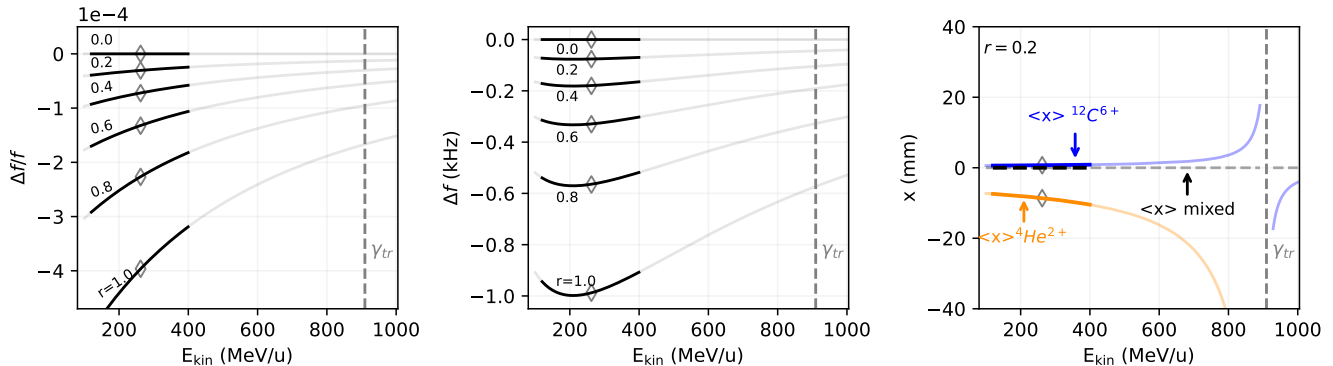


FIG. 3. Frequency and radial position offsets for mixed helium-carbon beams with different ion fractions r , estimated analytically (lines) and in simulations (grey diamond markers). The clinically relevant energy range is indicated by enhanced opacity. Left: relative frequency offsets with respect to a mono-isotopic $^{12}\text{C}^{6+}$ beam. Center: Absolute frequency offsets in a PIMMS synchrotron. Right: Horizontal centroid of the mixed, carbon, and helium charge distributions at the radial loop pick-up with $D_x = -8.3$ m. In this example the radial loop regulates to $x_{\text{RL}} = 0$ mm.

radial loop does not apply any frequency correction. Further, close to transition energy the presented method is no longer applicable due to large beam separation and related particle losses (see Fig. 3, right panel).

To validate Eqs. (23) and (24), simulations are performed with XSUITE [21], which enables tracking of particles with non-nominal charge-to-mass ratios. Details are outlined in Sec. A. In these simulations, Δf is determined numerically by enforcing the charge-weighted average radial displacement $\langle x \rangle_{\text{q,mix}}$ to be x_{RL} . As substitute for a radial feedback loop, the required frequency offset Δf is determined using the Nelder–Mead optimization algorithm [22], implemented in SciPY [23]. The resulting frequency offsets and the corresponding radial displacements are shown as gray diamond markers in Fig. 3, in excellent agreement with the expected values.

IV. EXPERIMENTAL DEMONSTRATION

The proposed method for estimating the ion fraction of dual-species beams was experimentally tested in 2025 at MedAustron Ion Therapy and Research Center.

A. Setup and measurement campaign

For this purpose, the helium fraction of mixed $^4\text{He}^{2+}$ and $^{12}\text{C}^{6+}$ beams was determined both at flat top in the synchrotron (Sec. IV A 2) and independently after extraction in the research irradiation room (Sec. IV A 2), as illustrated in Fig. 4. Measurements were performed at two extraction energies, 262.3 MeV/u and 402.8 MeV/u. For 262.3 MeV/u, measurements were carried out with two distinct radial loop setpoints, $x_{\text{RL}} = 27.5$ mm and 29.9 mm. For each energy and radial loop configuration, the ion fraction was varied by means of adapting the sequential injection settings (Sec. IV A 1). For each setting,

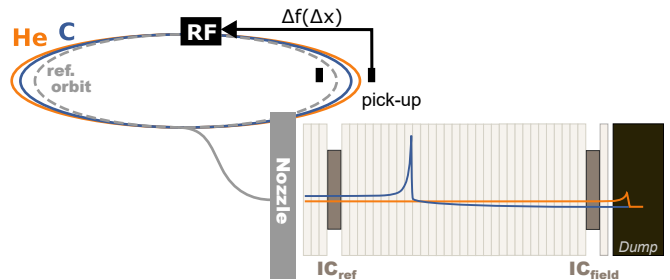


FIG. 4. Schematic of the two complementary methods to determine the ion composition of the dual-species beam: the non-invasive RF-based measurement in the synchrotron and the post-extraction measurement with an ionization-chamber (IC) telescope.

five measurements were performed.

1. Mixed beam delivery

The mixed beams were produced using the double multiturn injection scheme described in Sec. II A. Different ion fractions were obtained by varying the amplitude of the second injection bump, which is used for the injection of $^{12}\text{C}^{6+}$ ions. As a full calibration of the bump amplitude was not available at the time of writing, the bump strength is specified in terms of the injection bump current. By adjusting the injection kicker current between $I_{\text{MKI}} = 350$ and 0 A ion fractions ranging from $r = 0$ (pure $^{12}\text{C}^{6+}$) to $r = 1$ (pure $^4\text{He}^{2+}$) were achieved.

Slow extraction to the experimental room was performed using PDE, in which the beam is driven into the third-order resonance by sweeping an empty RF bucket through a coasting beam stack. PDE was used because the clinically employed betatron core is currently not compatible with mixed-species extraction [4], and the experimentally available RFKO system was not available

for the extraction at the time of the measurements.

For all measurements, the extraction parameters were chosen to extract the beam over ≈ 7 s while ensuring complete emptying of the synchrotron and avoiding saturation of the ionization chambers in the research irradiation room. For both beam energies, the empty RF bucket was empirically initialized at a frequency offset that did not induce beam losses upon application of RF voltage. A combination of RF voltage, i.e. bucket height, and frequency sweep speed was then empirically selected to empty the entire synchrotron over several seconds.

The extraction efficiency was estimated for pure $^{12}\text{C}^{6+}$ beams by comparing intensity measurements in the synchrotron with readings from the ionization chambers in the nozzle of the MedAustron research irradiation room. This yielded extraction efficiencies of $96.1 \pm 0.7\%$ for 262.3 MeV/u with a 27.5 mm radial loop offset, $95.6 \pm 0.6\%$ for 262.3 MeV/u with a 29.9 mm offset, and $96.0 \pm 0.2\%$ for 402.8 MeV/u with a 25 mm offset. However, operation in mixed-beam mode may lead to species-dependent changes in extraction efficiency relative to the reference measurements obtained with a pure carbon beam, which should therefore be taken into account when interpreting the results.

2. Measuring the ion composition in the synchrotron

Figure 5 shows representative low-level RF (LLRF) acquisitions used for the RF-based ion fraction quantification. As expected, the mixed $^4\text{He}^{2+}/^{12}\text{C}^{6+}$ beam (black) exhibits a frequency offset that lies between those of the two pure species (orange and blue). The respective frequency values required for the mixing ratio quantification were obtained by time-averaging the acquired RF frequency signal over a fixed time interval during the flat top period prior to extraction (grey-shaded region in Fig. 5). In the presented measurements, these intervals were 18 ms for 262.3 MeV/u beams and 6 ms for 402.8 MeV/u beams. These time windows were selected as the longest intervals at the end of the LLRF acquisition during which the frequency averages remained unaffected by residual magnetic field settling. The intervals are relatively short for the data presented because the main dipole magnets were operated in current-regulated mode, and the magnetic field had not yet fully stabilized by the end of the LLRF acquisition.

For each configured energy and radial loop setpoint, the reference frequency f_{ref} (f in Eq. (23)) and corresponding standard error $\sigma_{f_{\text{ref}}}$ were determined at the beginning of the measurement campaign by averaging 5 independent acquisitions with a pure $^{12}\text{C}^{6+}$ beam. The obtained rms frequency spread is $\sigma_{f_{\text{ref}}} < 8$ Hz for all extraction energies and radial loop offsets, which is therefore adopted as common uncertainty for all cases. This spread is mainly attributed to noise in the RF frequency read-out and to magnetic field fluctuations of the main dipole magnets operated in current-regulated mode.

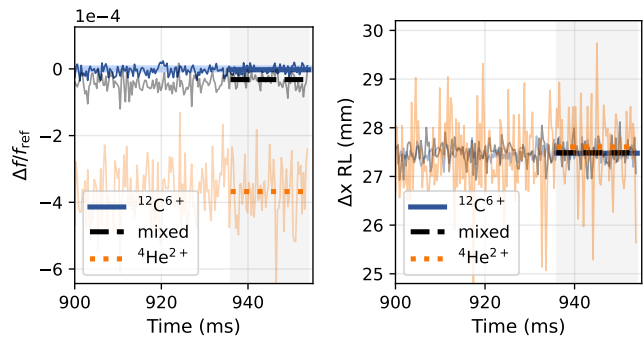


FIG. 5. LLRF acquisitions at flat top for 262.3 MeV/u $^{12}\text{C}^{6+}$, $^4\text{He}^{2+}$ and mixed beams, with the radial loop regulating to $x_{\text{RL}} = 27.5$ mm. The gray-shaded time window is used to determine the average frequencies, shown by the solid lines. Left: Relative RF frequency offset with respect to a pure $^{12}\text{C}^{6+}$ beam. The blue-shaded band marks the reference frequency $f_{\text{ref}} \pm 3\sigma_{f_{\text{ref}}}$. Right: Position measured at the radial loop pick-up.

The blue-shaded band in the left subplot of Fig. 5 represents the resulting $^{12}\text{C}^{6+}$ reference frequency interval of $\pm 3\sigma_{f_{\text{ref}}}$.

For each subsequent mixed beam measurement, the revolution frequency f_{mix} is measured, the corresponding frequency shift $\Delta f = f_{\text{mix}} - f_{\text{ref}}$ calculated, and the ion fraction r obtained via Eq. (24).

Figure 5 further shows that the frequency fluctuations are noticeably larger for the pure $^4\text{He}^{2+}$ beam than for the mixed and pure $^{12}\text{C}^{6+}$ beams. This is attributed to the lower helium beam current and to the gain setting of the pick-up amplifier, which is optimized for $^{12}\text{C}^{6+}$ operation. This results in less stable regulation for beams with $r \rightarrow 1$. Nevertheless, the measurement quality is sufficient for the presented proof-of-principle demonstration. Importantly, the pick-ups installed in the MedAustron synchrotron are of the shoe-box type, which provide a linear relationship between beam displacement and induced signal over a wide displacement range [18], as implied by the presented model.

Representative parameter sets and the corresponding rms uncertainties used for error propagation are listed in Table I. The uncertainty of the extraction energy is conservatively assumed to be 3 MeV/u to account for non-nominal synchrotron operation in the mixed beam setup. However, its effect is negligible, as the uncertainty in Δf is the dominant contribution to the uncertainty in r .

3. Measuring the ion composition of the extracted beam

a. Methodology: In the research irradiation room, a two-stage ionization chamber (IC) telescope was used to quantify the mixing ratio of the extracted beam. As illustrated in Fig. 4, the two ICs are positioned at different penetration depths, with the *reference chamber* IC_{ref} be-

TABLE I. Parameters for the helium fraction quantification using the synchrotron RF-based method and the ionization chamber telescope.

263.2 MeV/u		27.5 mm radial offset	
Parameter	Value	Standard error	Unit
f_{ref}	$2.405\,142 \times 10^6$	8	Hz
Δf	$\Delta f(r) \in [0, -1000]$	8	Hz
E_{kin}	263.2	3	MeV/u
a_{He}	1.54	4×10^{-3}	-
a_{C}	0.01	2×10^{-5}	-
ΔE_{He}	5.69×10^{-3}	5%	MeV
ΔE_{C}	5.45×10^{-2}	5%	MeV

402.8 MeV/u		25 mm radial offset	
Parameter	Value	Standard error	Unit
f_{ref}	$2.757\,010 \times 10^6$	8	Hz
Δf	$\Delta f(r) \in [0, -900]$	8	Hz
E_{kin}	402.8	3	MeV/u
a_{He}	0.77	2×10^{-3}	-
a_{C}	0.15	5×10^{-4}	-
ΔE_{He}	4.53×10^{-3}	5%	MeV
ΔE_{C}	4.07×10^{-2}	5%	MeV

ing located in the entrance plateau of the carbon Bragg peak, while the *field chamber* IC_{field} is located in between the $^{12}\text{C}^{6+}$ and the $^4\text{He}^{2+}$ Bragg peaks. The ion composition can be reconstructed from the ratio of the currents measured simultaneously on both ICs, I_{ref} and I_{field} [24].

The method relies on calibration factors that relate the average signal induced by a primary $^4\text{He}^{2+}$ or $^{12}\text{C}^{6+}$ ion, or by their fragments, in IC_{field} to the corresponding signal in IC_{ref}. These factors are determined in dedicated calibration measurements performed at the beginning of the experiment by irradiating the IC telescope with pure helium and pure carbon beams and computing

$$a_j = \frac{I_{\text{field},j}}{I_{\text{ref},j}} \quad j = \text{He and C} . \quad (30)$$

To first order, these calibration factors are independent of the incident beam intensity.

During measurements with the mixed-species beam, the total current in the two ICs is

$$\begin{aligned} I_{\text{ref}}(t) &= I_{\text{ref,He}}(t) + I_{\text{ref,C}}(t) \\ I_{\text{field}}(t) &= I_{\text{field,He}}(t) + I_{\text{field,C}}(t) , \end{aligned} \quad (31)$$

where t describes the time during the ≈ 10 s spill. Using the calibration factors defined in Eq. (30), the current in the field IC can be written as

$$I_{\text{field}}(t) = a_{\text{He}} I_{\text{ref,He}}(t) + a_{\text{C}} I_{\text{ref,C}}(t). \quad (32)$$

Solving this system of equations yields

$$\begin{aligned} I_{\text{ref,He}}(t) &= \frac{I_{\text{field}}(t) - a_{\text{C}} I_{\text{ref}}(t)}{a_{\text{He}} - a_{\text{C}}} \\ I_{\text{ref,C}}(t) &= \frac{a_{\text{He}} I_{\text{ref}}(t) - I_{\text{field}}(t)}{a_{\text{He}} - a_{\text{C}}}. \end{aligned} \quad (33)$$

The integrated reference IC current for each species j over the spill duration T is

$$I_{\text{ref},j} = \sum_{i=0}^{T/\Delta t} I_{\text{ref},j}(t_i) \Delta t , \quad (34)$$

where Δt is the sampling time of the electrometer. The fraction of extracted ions per species is subsequently obtained from the ratio of these integrated currents and the ratio $\Delta E_{\text{He}}/\Delta E_{\text{C}}$ of the energy deposited in the detector volume per primary $^4\text{He}^{2+}$ and $^{12}\text{C}^{6+}$ ion for the given experimental configuration,

$$\frac{N_{\text{He}}}{N_{\text{C}}} = \frac{I_{\text{ref,He}} \Delta E_{\text{C}}}{I_{\text{ref,C}} \Delta E_{\text{He}}}. \quad (35)$$

The ion fraction r then follows as

$$r = \frac{\frac{N_{\text{He}}}{N_{\text{C}}}}{\frac{N_{\text{He}}}{N_{\text{C}}} + 1}. \quad (36)$$

$\Delta E_{\text{He}}/\Delta E_{\text{C}}$ is obtained from OPENGATE [25] simulations, with details described below.

b. Details on the experimental setup: The presented experiment employed PTW 34070 ICs, separated in range by multiple PTW RW3 absorber plates (PTW Freiburg GmbH, Freiburg, Germany). The reference chamber was positioned after 3 plates, with another 33 plates installed in between reference and field IC. Each plate has a physical thickness of 1 cm. Their water equivalent thickness has been characterized with protons and is available internally at the MedAustron facility. Both ICs fully covered the entire beam, which was verified using Gafchromic™ EBT3 radiochromic films (Ashland Inc., Wayne, NJ, USA) upstream and downstream of the IC telescope. This configuration assured that the carbon Bragg peak position (around 14 cm for 262.3 MeV/u and 28 cm for 402.8 MeV/u) was in between the two ICs for both energies while the $^4\text{He}^{2+}$ Bragg peak (approximately 41 cm for 262.3 MeV/u and 83 cm for 402.8 MeV/u) was located after the field IC. The ICs were read out with a 50 ms integration time using a PTW TANDEM dual channel electrometer.

The setup specific parameters and the corresponding rms uncertainties used for error propagation are summarized in Table I. The calibration factors a_{He} and a_{C} were obtained by averaging five acquisitions taken at the beginning of the measurement campaign. To obtain ΔE_{He} and ΔE_{C} , a simplified model of the setup was simulated in OPENGATE (version 10.0.3 using GEANT4 [26] version 11.2.3). The PTW RW3 slabs were implemented explicitly according to their material composition. The active region of the ICs was modeled as 2 mm air-filled volumes with energy deposition scored over the full sensitive detector thickness and cross section. The simulations employed the GEANT4 SHIELDING_EMZ physics list [27], which provides stopping-power data based on the ICRU

Report 90 [28] for protons, alpha particles, and heavy ions in water, graphite, and air. Given the high energies of the helium and carbon ions and the low fragmentation upstream of the reference IC, the ICRU90 stopping-power data are expected to dominate the energy-loss modeling in the detector volumes. This study assumes an rms error of 5% for the estimate on the deposited energy ΔE . On the one hand, this value contains systematic uncertainties related to stopping power data, which are assumed to be $\pm 2.5\%$ in accordance with recent comparisons of stopping powers obtained with different GEANT4 physics lists [29]. Further, the error budget accounts for statistical simulation uncertainties ($< 1\%$) and systematic errors in the simulation setup. A more precise quantification of these uncertainties is subject to future studies and goes beyond the presented proof of principle.

4. Data analysis

To quantify potential systematic differences between the two independent ion fraction estimates, a simple phenomenological model is introduced. For each method the inferred helium fraction is written as

$$r_i = \frac{\lambda_i N_{\text{He}}}{\lambda_i N_{\text{He}} + N_{\text{C}}}, \quad i = \text{ic, rf} \quad (37)$$

where N_{He} and N_{C} denote unknown ground truth, i.e. the intensities prior to both measurements. λ_i accounts for method-specific response differences, such as species-dependent quantification or extraction efficiencies.

Eliminating N_{He} and N_{C} yields a direct relation between the ion fraction estimates of both methods. Defining

$$\kappa = \frac{\lambda_{\text{ic}}}{\lambda_{\text{rf}}}, \quad (38)$$

the expected relation reads

$$\widehat{r}_{\text{rf}}(r_{\text{ic}}) = \frac{\kappa r_{\text{ic}}}{(1 - r_{\text{ic}}) + \kappa r_{\text{ic}}}. \quad (39)$$

In the presented measurements, the parameter κ was determined by ordinary least-squares regression. Pure-species points ($r = 0$, $r = 1$) are, by design, detected as such by the IC setup, independent of detection and extraction efficiencies. These data points were excluded from the fit. The fitted parameter κ represents an effective relative response between the two methods, incorporating differences in detection and extraction efficiencies for the presented measurement setup. The adequacy of this model was assessed using the residuals $r_{\text{rf}} - \widehat{r}_{\text{rf}}(r_{\text{ic}})$.

B. Experimental results

The ion fractions r estimated using the two different methods are compared in Fig. 6. The left panels show

a direct comparison between the ion fraction of the extracted beam measured in the research irradiation room (x-axis, r_{ic}), and the non-invasive composition estimate obtained in the synchrotron (y-axis, r_{rf}). The colored markers correspond to different injection settings used to tailor the ion fraction.

For a fixed injection setting, i.e. one color in Fig. 6, the measured ion fractions exhibit significant fluctuations in selected cases. The fact that these variations are consistently reflected in both methods indicates that these are real shot-to-shot fluctuations of the beam composition rather than measurement artifacts.

Importantly, the pure-species limit $r = 1$, which is intrinsically identified as such by the IC-based measurement, is also recovered as $r \approx 1$ by the RF-based method. This agreement provides a strong consistency check of the underlying model, as it follows directly from the calculated frequency offset rather than from any interpolation.

At intermediate ion fractions, deviations between the two methods are observed. The fit of the model in Eq. (39) yields a value of $\kappa \approx 0.75$ to 0.83 for the different measurement sets. This indicates a difference in the relative response to the initially present ${}^4\text{He}^{2+}$ and ${}^{12}\text{C}^{6+}$ between the two methods, which may arise from species-dependent detection efficiencies and/or differences in extraction efficiency. The deviations are largest at intermediate ion fractions ($r \approx 0.5$), where $\kappa \approx 0.8$ corresponds to the in-synchrotron measurement yielding a helium fraction that is approximately up to 6% lower than that inferred from the ICs in the experimental room. However, as the present results serve as a proof of principle, the regression is used only to assess systematic trends. A detailed quantitative and physical discussion of the fit parameters is deferred to future studies.

The corresponding residuals of the fitted model are shown in the right panels. For all investigated configurations, the residuals are centered around zero and remain within approximately $\pm 7\%$, with no significant systematic trends observed over the full range, supporting the validity of the model parameterized by κ , Eq. (39).

V. DISCUSSION AND OUTLOOK

A. Method applicability and limitations

The presented results demonstrate the feasibility of non-invasively estimating the ion composition of dual-species beams directly in the synchrotron, with good agreement between the RF-based method and the IC telescope. While the current implementation is not intended for high-precision measurements, it already provides significant practical value and is routinely used for mixed beam commissioning and experiments. In many experimental scenarios, the installation of an IC telescope is not compatible with the experimental setup. In such cases, the presented non-invasive approach enables cycle-resolved approximate composition monitoring

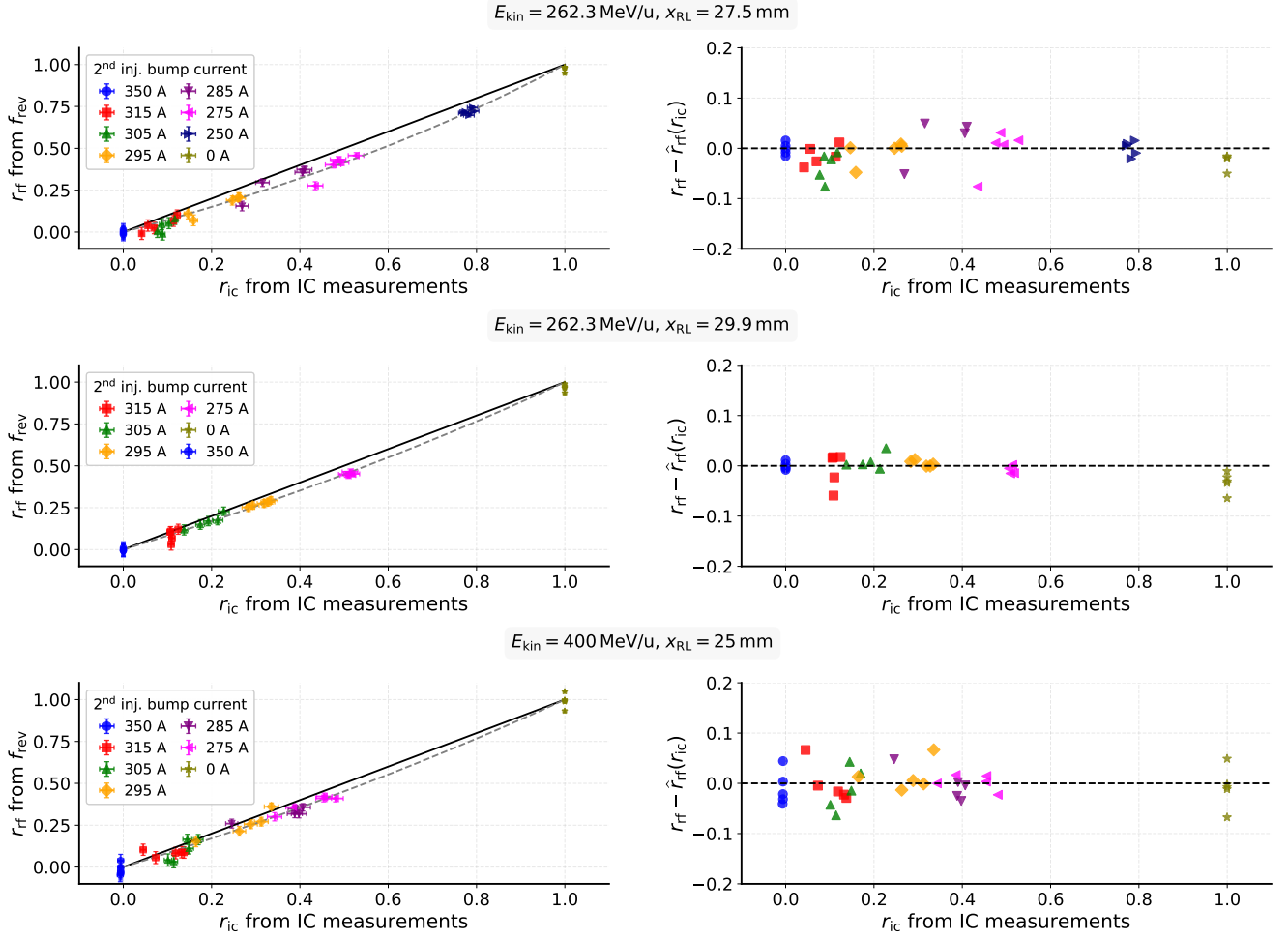


FIG. 6. Left: Comparison of the ion fraction obtained with the ionization chamber telescope in the irradiation room (x-axis) and the non-invasive RF-based quantification in the synchrotron (y-axis) for different beam energies and radial loop offsets. The black solid line indicates the identity $r_{\text{ic}} = r_{\text{rf}}$, the gray dashed line shows the linear fit based on the efficiency model. Right: Residuals of the fit.

without interfering with beam delivery.

Further improvements in accuracy are expected from including direct magnetic field measurements or B -field regulation of the main dipole magnets, which would suppress frequency errors caused by field fluctuations. Further, a longer RF frequency acquisition time at constant magnetic field could reduce statistical fluctuations. In addition, potential differences in extraction efficiency between the two ion species as well as the precision and accuracy of the IC telescope require further investigation to facilitate an improved quantitative interpretation of the agreement between the two methods.

B. Operational implications of radial loop regulation for mixed-species beams

The frequency correction applied by the radial loop for a given ion composition, Eq. (23), induces a composition-

dependent shift in $\beta\gamma$ and, consequently, in the flat top energy of the reference ion species which is used for tumor treatment. For a PIMMS-like synchrotron operated with mixed ${}^4\text{He}^{2+}/{}^{12}\text{C}^{6+}$ beams, mixing ratios up to $r \leq 0.4$ would result in flat top energy shifts below $\Delta E_{\text{kin}} = 0.17 \text{ MeV/u}$ over the entire clinical energy range. The stated value represents the largest shift and occurs at 400 MeV/u. When extracting the beam using the amplitude-driven slow extraction mechanism RFKO, this energy offset is also maintained during the extraction and delivered to the irradiation room. For prospective clinical implementation, these energy offsets must be compared with the energy and range tolerances permitted during nominal operation in ion beam therapy. A typical tolerance for ${}^{12}\text{C}^{6+}$ beams is $\pm 0.25 \text{ MeV/u}$ at 400 MeV/u, with larger allowable energy deviation for lower energies [30]. This first estimate indicates that even for mixing ratios of $r = 0.4$, which is well above the expected operational range of $r = 0.1$ to 0.2 for mixed

${}^4\text{He}^{2+}/{}^{12}\text{C}^{6+}$ beams, the resulting energy shifts remain within the acceptable tolerance.

Nevertheless, a more precise quantification of these effects and their experimental validation are recommended for future studies. Such studies should not only quantify the expected shifts in flat top and extraction energy for different extraction mechanisms, but also assess the implications for energy verification systems, such as systems based on RF readout at flat top. At the same time, the presented results indicate that such verification schemes could, in principle, be used to monitor ion composition and to generate interlocks in the case of non-nominal mixing ratios. Such systems could benefit from direct integration of the ion fraction determination into the LLRF system. Further studies of the feasibility of such an approach are recommended.

VI. CONCLUSION

We have demonstrated a practical, non-invasive method to determine the ion composition of dual-species beams with charge-to-mass offsets of order 10^{-4} in low-energy synchrotrons with radial RF regulation loops. An analytical model was derived that relates RF frequency offsets to ion fractions. The method was validated with XSUITE tracking simulations and demonstrated experimentally at MedAustron, where the RF-based mixing ratio estimates were found to be in good agreement with independent ion composition estimates of the extracted beam.

The method is now used at MedAustron for mixed beam commissioning and diagnostics during user experiments. It offers potential for developing a mixing ratio interlock system, with further improvements in accuracy expected under optimized measurement conditions.

VII. ACKNOWLEDGMENTS

The financial support of the Austrian Ministry of Education, Science, and Research is gratefully acknowledged for providing beam time and research infrastructure at MedAustron. Further, part of the research underlying this work was funded as part of the RTI-Strategy Lower Austria 2027. The authors would like to warmly thank the colleagues from the OPS and TBU department of MedAustron, in particular C. Schmitzer for collaboration on the mixed beam project as well as L. Adler, L. Fuxreiter, N. Gambino, T. Gere, T. Margreiter, F. Plassard, D. Prokopovich, V. Rizzoglio, M. Sakelsek, M. Walter and M. Wolf, for their support with measurements at the MedAustron synchrotron. We are further very grateful to D. Ondreka (GSI) for invaluable discussions on the presented formalism, as well as F. Ulrich-Pur (TU Wien), M. Pullia (CNAO), and A. Pastushenko (GSI) for general collaboration on mixed beam delivery and detection concepts. We also thank D. Prokopovich, D. Ondreka and

C. Schmitzer for providing feedback on the manuscript.

VIII. AUTHOR CONTRIBUTIONS

Conceptualization: E. Renner; Methodology: E. Renner, M. Kausel, H. Fuchs; Investigation: E. Renner, M. Kausel, K. Holzfeind, N. Okropiridze; Formal analysis: E. Renner, N. Okropiridze; Writing - original draft: E. Renner; Writing - review & editing: E. Renner, M. Kausel, K. Holzfeind, H. Fuchs, N. Okropiridze.

IX. DATA AVAILABILITY

All raw data are not publicly available upon publication because it is not technically feasible and/or the cost of preparing, depositing, and hosting the data would be prohibitive within the terms of this project. The data are available from the authors upon reasonable request.

Appendix A: Validation with Xsuite simulations

Equations (23) and (24) are validated using the the beam dynamics simulation framework XSUITE [21], which allows for tracking of particles with non-nominal q/m . The simulations employed `xtrack` v0.89.4 and are used to numerically determine the revolution frequency offset Δf , which is required to regulate the charge-weighted radial displacement $\langle x \rangle_{q,\text{mix}}$ to a specified x_{RL} for mixed ${}^4\text{He}^{2+}/{}^{12}\text{C}^{6+}$ beams with ion fractions $r = 0$ to 1. The simulations are prepared by initializing a generic PIMMS lattice with an on-momentum ${}^{12}\text{C}^{6+}$ as reference particle and $E_{\text{kin}} = 262.3 \text{ MeV/u}$ as reference energy. This reference particle moves on a closed orbit with length C , and features the revolution frequency f and the relativistic factors β and γ .

As a substitute for an explicit radial feedback loop, the required RF frequency offset Δf is determined using the Nelder-Mead optimization algorithm [22], as implemented in SCIPY [23]. The algorithm varies Δf to minimize the cost function

$$C = \left| \langle x \rangle_{q,\text{mix}} - \Delta x_{\text{RL}} \right|. \quad (\text{A1})$$

Each iteration of the optimization proceeds as follows.

- (1) *Application of an RF frequency shift:* In XSUITE, applying a shifted frequency $f_{\text{RF}} = f + \Delta f$ not only implies that this value is assigned as new frequency to the `xtrack.Cavity` element, but also that a corresponding shift in the longitudinal coordinate ζ ,

$$\Delta \zeta = C \frac{\Delta f}{f}, \quad (\text{A2})$$

is assigned via `dzeta` of the `xtrack.ZetaShift` element. The latter is the standard method for programming off-momentum operation and inducing radial orbit offsets in XSUITE [31].

- (2) *Initialization of a $^{12}\text{C}^{6+}$ test particle close to the synchronous $^{12}\text{C}^{6+}$ particle:* The test particle is initialized with the longitudinal phase space coordinates $(\zeta_{\text{C}}, \delta_{\text{C}}) = \left(0, -\frac{\Delta f/f}{\eta}\right)$, with η being the linear slippage factor. Due to numerical and linearization errors, the test particle is initialized close to, but not exactly on, the phase space coordinates of the synchronous particle and therefore performs small synchrotron oscillations around it. Since the test particle will be tracked over multiple synchrotron periods in step (5), these small initial offsets will not affect the averaged solution.
- (3) *Initialization of a $^4\text{He}^{2+}$ test particle close to the synchronous $^4\text{He}^{2+}$ particle:* The initial momentum deviation of $^{12}\text{C}^{6+}$, δ_{C} , is then used to compute γ_{C} , β_{C} and eventually the offset δ_{sp} between

$^4\text{He}^{2+}$ and $^{12}\text{C}^{6+}$ with Eq. (11). Subsequently β_{He} , obtained via Eq. (10), is used to determine the momentum deviation δ_{He} of $^4\text{He}^{2+}$ with respect to the lattice reference particle. The $^4\text{He}^{2+}$ test particle is initialized with the longitudinal phase space coordinates $(\zeta_{\text{He}}, \delta_{\text{He}}) = (0, \delta_{\text{He}})$.

- (4) *Tracking and estimation of radial loop offset:* Both test particles are tracked over multiple synchrotron periods. The average radial displacements at the radial loop pick-up, $\langle x \rangle_{\text{C}}$ and $\langle x \rangle_{\text{He}}$, are obtained by averaging the respective offsets over multiple synchrotron periods, thereby averaging out radial oscillations arising from small-amplitude synchrotron motion. For a given ion fraction r , $\langle x \rangle_{\text{q,mix}}$ is subsequently computed using Eq. (18).
- (5) *Computation of cost function:* The cost function \mathcal{C} , Eq. (A1), is evaluated and returned to the optimization algorithm, which iteratively updates Δf until convergence is achieved.

-
- [1] C. Graeff, U. Weber, C. Schuy, N. Saito, L. Volz, P. Pierimoni, J. Seco, and M. Kraemer, *Helium as a range probe in carbon ion therapy*, *Physica Medica: European Journal of Medical Physics* **52**, 11 (2018).
 - [2] D. Mazzucconi, S. Agosteo, M. Ferrarini, L. Fontana, V. Lante, M. Pullia, and S. Savazzi, *Mixed particle beam for simultaneous treatment and online range verification in carbon ion therapy: Proof-of-concept study*, *Medical Physics* **45**, 5234–5243 (2018).
 - [3] M. Galonska, W. Barth, C. Graeff, R. Hollinger, F. Maimone, D. Ondreka, S. Reimann, M. Schanz, J. Stadlmann, P. Spiller, D. Varentsov, L. Volz, and T. Wagner, *First dual isotope beam production for simultaneous heavy ion radiotherapy and radiography*, in *Proceedings of the 15th International Particle Accelerator Conference* (JACoW Publishing, Geneva, Switzerland, 2024) pp. 1893–1896.
 - [4] M. Kausel, C. Schmitzer, A. Gsponer, M. Wolf, H. Fuchs, F. Ulrich-Pur, T. Bergauer, A. Hirtl, N. Gambino, and E. Renner, *Double multiturn injection scheme for generating mixed helium and carbon ion beams at medical synchrotron facilities*, *Phys. Rev. Accel. Beams* **28**, 111001 (2025).
 - [5] J. J. Hardt, A. A. Pryanichnikov, O. Jäkel, J. Seco, and N. Wahl, *Helium range viability for online range probing in mixed carbon–helium beams*, *Medical Physics* **52**, e70194 (2025).
 - [6] L. Badano, M. Benedikt, P. J. Bryant, M. Crescenti, P. Holy, A. T. Maier, M. Pullia, S. Rossi, and P. Knaus, *Proton-Ion Medical Machine Study (PIMMS)*, **1**, Technical Report No. CERN-PS-99-010-DI (CERN, Geneva, Switzerland, 2000).
 - [7] P. J. Bryant, L. Badano, M. Benedikt, M. Crescenti, P. Holy, A. T. Maier, M. Pullia, S. Reimoser, S. Rossi, G. Borri, P. Knaus, F. Gramatica, M. Pavlovic, and L. Weisser, *Proton-Ion Medical Machine Study (PIMMS)*, **2**, Technical Report No. CERN-PS-2000-007-DR (CERN, Geneva, Switzerland, 2000).
 - [8] C. Schmitzer, A. Farinon, F. Garonna, M. Kronberger, T. Kulenkampff, C. Kurfürst, S. Myalski, S. Nowak, F. Osmić, L. Penescu, M. Pivi, P. Urschütz, and A. Wastl, *MedAustron Synchrotron RF Commissioning for Medical Proton Beams*, in *Proceedings of the 7th International Particle Accelerator Conference* (JACoW Publishing, Geneva, Switzerland, 2016) pp. 844–846.
 - [9] A. De Franco, L. Adler, F. Farinon, N. Gambino, G. Guidoboni, G. Kowarik, M. Kronberger, C. Kurfürst, S. Myalski, S. Nowak, M. T. F. Pivi, C. Schmitzer, I. Strašák, P. Urschütz, and A. Wastl, *Slow Extraction Optimization at the MedAustron Ion Therapy Center: Implementation of Front End Acceleration and RF Knock Out*, in *Proceedings of the 9th International Particle Accelerator Conference* (JACoW Publishing, Geneva, Switzerland, 2018) pp. 453–456.
 - [10] F. Kühleubl, *Slow Extraction Optimisation for the MedAustron Synchrotron*, *Ph.D. thesis*, TU Wien, Vienna, Austria (2024).
 - [11] E. Renner, A. Gsponer, C. Schmitzer, D. Prokopovich, F. Plassard, F. Kuehteubl, K. Knoll, and S. Waid, *Investigating pulsed slow extraction schemes at the MedAustron synchrotron*, in *Proceedings of the 15th International Particle Accelerator Conference* (JACoW Publishing, Geneva, Switzerland, 2024) pp. 3595–3598.
 - [12] P. D. Hermes, *Heavy-Ion Collimation at the Large Hadron Collider: Simulations and Measurements*, *Ph.D. thesis*, University of Münster, Münster, Germany (2016).
 - [13] P. J. Bryant and K. Johnsen, *The Principles of Circular Accelerators and Storage Rings*, 1st ed. (Cambridge University Press, 1993).
 - [14] N. Angert, E. Brouzet, R. Garoby, S. Hancock, H. Haseroth, C. Hill, K. Schindl, and P. Tetu, *Accelerating and separating mixed beams of ions with similar*

- charge to mass ratio in the CERN PS complex, in *Proceedings of the 1st European Particle Accelerator Conference* (JACoW Publishing, Geneva, Switzerland, 1988) pp. 1367–1369.
- [15] K. Holzfeind, *Implementation of longitudinal phase space tomography at MedAustron*, *Diploma thesis*, TU Wien, Vienna, Austria (2024).
- [16] E. Renner, M. Kausel, F. Plassard, F. Kuehteubl, C. Schmitzer, M. Wolf, and V. Kirchweger, *Towards the slow extraction of mixed He-2+ and C-6+ beams for on-line range verification*, in *Proceedings of the 15th International Particle Accelerator Conference* (JACoW Publishing, Geneva, Switzerland, 2024) pp. 3597–3600.
- [17] S. Hancock, *Transition Revisited*, Technical Report No. CERN-PS-90-53-OP (CERN, Geneva, 1990).
- [18] P. Strehl, *Beam Instrumentation and Diagnostics*, Particle Acceleration and Detection (Springer, Berlin, 2006).
- [19] S. van der Meer, *Measuring the $p - \bar{p}$ mass difference by the transition energy method*, Technical Report No. CERN-PS-AA-78-17 (CERN, Geneva, 1978).
- [20] M. T. F. Pivi, L. Adler, A. De Franco, F. Farinon, N. Gambino, G. Guidoboni, G. Kowarik, M. Kronberger, C. Kurfürst, H. T. Lau, S. Myalski, S. Nowak, L. Penescu, C. Schmitzer, I. Strašák, P. Urschütz, and A. Wastl, *Status of the Carbon Commissioning and Roadmap Projects of the MedAustron Ion Therapy Center Accelerator*, in *Proceedings of the 10th International Particle Accelerator Conference* (JACoW Publishing, Geneva, Switzerland, 2019) pp. 3404–3407.
- [21] G. Iadarola *et al.*, *Xsuite: An Integrated Beam Physics Simulation Framework*, in *Proceedings of the 68th ICFA Advanced Beam Dynamics Workshop on High-Intensity and High-Brightness Hadron Beams*, Vol. 68 (JACoW Publishing, Geneva, Switzerland, 2024) pp. 73–80.
- [22] J. A. Nelder and R. Mead, *A simplex method for function minimization*, *The Computer Journal* **7**, 308–313 (1965).
- [23] P. Virtanen *et al.*, *SciPy 1.0: Fundamental Algorithms for Scientific Computing in Python*, *Nature Methods* **17**, 261–272 (2020).
- [24] M. Kausel, C. Schmitzer, K. Holzfeind, C. Becker, and E. Renner, *Recent developments in delivering mixed helium and carbon ion beams at MedAustron*, in *Proceedings of the 16th International Particle Accelerator Conference* (JACoW Publishing, Geneva, Switzerland, 2025) pp. 1147–1150.
- [25] D. Sarrut *et al.*, *The OpenGATE ecosystem for Monte Carlo simulation in medical physics*, *Physics in Medicine & Biology* **67**, 184001 (2022).
- [26] S. Agostinelli *et al.*, *Geant4—a simulation toolkit*, *Nuclear Instruments and Methods in Physics Research Section A: Accelerators, Spectrometers, Detectors and Associated Equipment* **506**, 250–303 (2003).
- [27] Geant4 Collaboration, *Guide For Physics Lists* (2025), release 11.4.
- [28] The International Commission on Radiation Units and Measurements, *Key Data for Ionizing-Radiation Dosimetry: Measurement Standards and Applications*, *Journal of the ICRU* **14**, 10.1093/jicru/ndw029 (2014), ICRU Report No. 90.
- [29] S. H. Lee, Y. Hirano, J. Son, *et al.*, *Influence of stopping power tables on carbon-ion range simulations in Geant4*, *Journal of the Korean Physical Society* **87**, 855–859 (2025).
- [30] F. Moser, *Energy verification in ion beam therapy*, *Phd thesis*, TU Wien, Vienna, Austria (2012).
- [31] Xsuite User’s Guide, *Off-momentum from RF frequency change*, accessed: 30-Dec-2025.